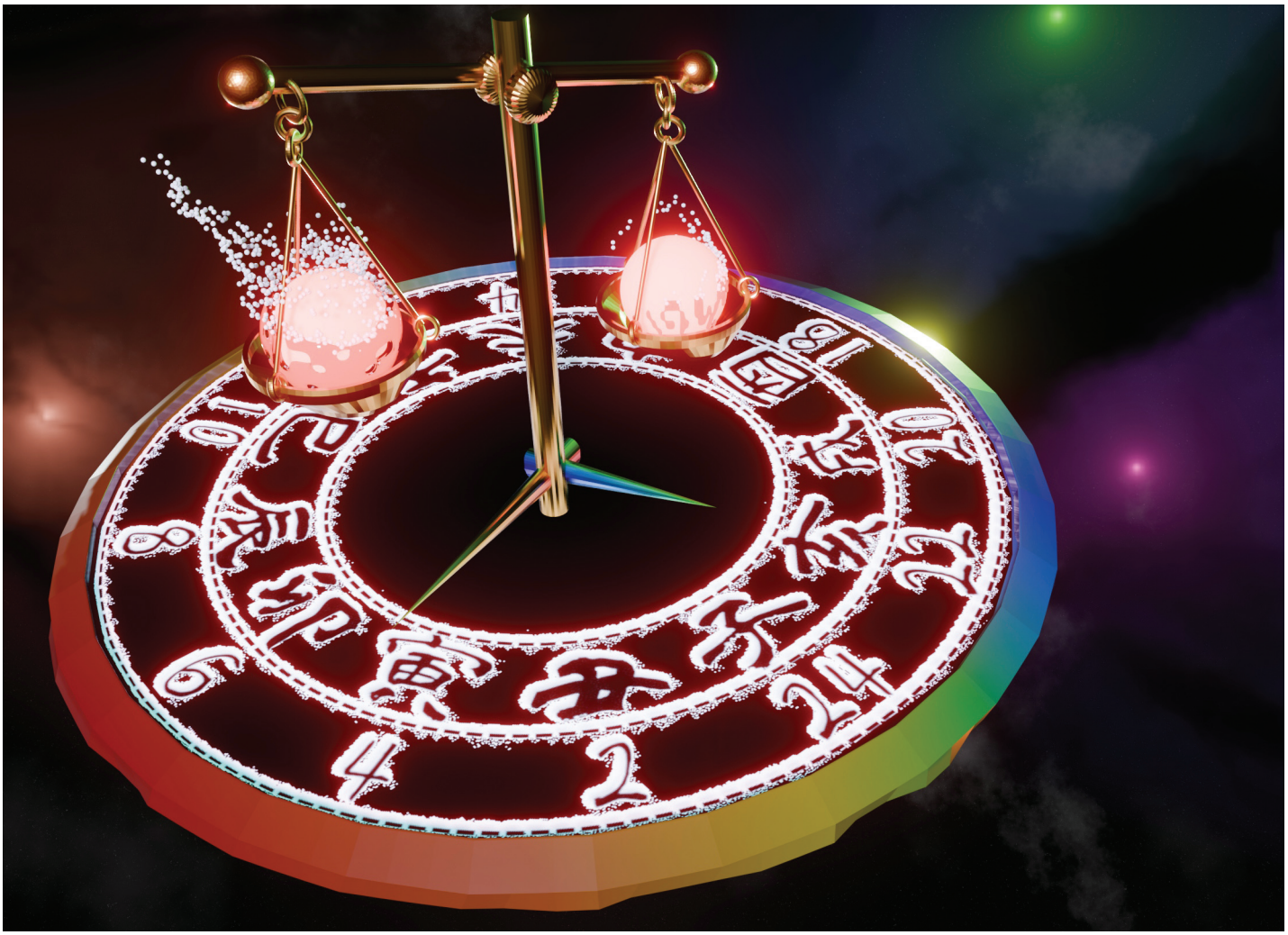

Showcasing research from Dr. Jonathan Veinot's group at the Chemistry Department, University of Alberta, Canada.

Not all silicon quantum dots are equal: photostability of silicon quantum dots with and without a thick amorphous shell

Colloidal silicon quantum dots (SiQDs) offer eco-friendly alternatives for optical applications, yet their structure's impact on photostability remains underexplored. This study compares the photostability of SiQDs with an amorphous shell with over-etched counterparts of equivalent dimensions that bore a negligible shell. UV degradation studies reveal a negative impact from the amorphous shell on the photoluminescence quantum yield. Our findings enhance comprehension of SiQD stability and offer insights into creating more sustainable luminescent systems.

As featured in:

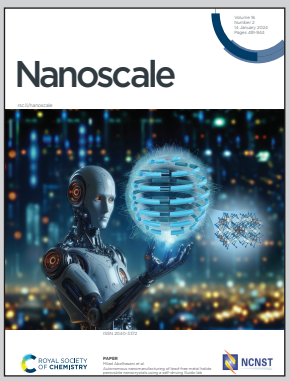

See Jonathan G. C. Veinot *et al.*, *Nanoscale*, 2024, **16**, 592.

ROYAL SOCIETY OF CHEMISTRY

rsc.li/nanoscale

Registered charity number: 207890

Nanoscale

ROYAL SOCIETY OF CHEMISTRY

PAPER

View Article Online
View Journal | View Issue

Cite this: *Nanoscale*, 2024, **16**, 592

Not all silicon quantum dots are equal: photostability of silicon quantum dots with and without a thick amorphous shell†

I Teng Cheong, [a] LiYifan Yang Szepesvari, [a] Chuyi Ni, [a] Cole Butler,[a] Kevin M. O'Connor, [a] Riley Hooper, [a] Alkiviathes Meldrum [b] and Jonathan G. C. Veinot *[a]

Luminescent colloidal silicon quantum dots (SiQDs) are sustainable alternatives to metal-based QDs for various optical applications. While the materials are reliant on their photoluminescence efficiency, the relationship between the structure and photostability of SiQDs is yet to be well studied. An amorphous silicon (a-Si) shell was recently discovered in SiQDs prepared by thermally-processed silicon oxides. As a-Si is known as a source of defects upon UV irradiation, the disordered shell could potentially have an adverse effect on the optical properties of nanoparticles. Herein, the photostability of ~5 nm diameter SiQDs with an amorphous shell was compared with that of over-etched SiQDs of equivalent dimensions that bore an a-Si shell of negligible thickness. An UV-induced degradation study was conducted by subjecting toluene solutions of SiQDs to 365 nm light-emitting diodes (LEDs) under an inert atmosphere for predetermined times up to 72 hours. The structure, composition, and optical responses of the exposed SiQDs were evaluated.

Received 5th September 2023,
Accepted 3rd December 2023

DOI: 10.1039/d3nr04478e

rsc.li/nanoscale

1. Introduction

Quantum dots are nanosized semiconductor particles that have tunable optical and electronic properties. Silicon quantum dots (SiQDs) are a subclass of these materials that exhibit luminescence throughout the visible to infrared spectral regions and tailorable surface functionalities.[1–4] The biocompatibility[5–7] and abundance of silicon make SiQDs even more attractive as promising alternatives for toxic heavy metals-containing nanoparticles.[8–10] Notably, various SiQD-based prototypes such as light-emitting diodes,[11–15] solar concentrators,[16–19] photodetectors,[20,21] biological labels,[22–25] and photocatalysts[26–28] have emerged. If SiQDs are to realize their full practical utility in these, and other far-reaching applications, it is essential that photoluminescence (PL) maxima tunability, narrow emission bandwidth, and high quantum yield (QY) be achieved while maintaining long-term stability.

The photoluminescence maximum of SiQDs is size dependent and is influenced by the confinement of charged carriers in geometric dimensions of the particles (*i.e.*, quantum confinement).[1,29–34] Synthesis methods such as thermal pyrolysis of silicon oxides,[35–40] nonthermal plasma synthesis from appropriate precursors,[41–45] and pulsed laser ablation of silicon percursors[46–48] have been developed and all provide some measure of control over the SiQD sizes, and by extension, tailorability of the PL maxima. The corollary to this size-based tuning is the unique opportunity to manipulate SiQD emission maximum through the exploitation of surface-state-mediated relaxation involving surface heteroatoms (*e.g.*, N, O, halides, *etc*).[4,49–51] Single-dot spectroscopy of individual SiQDs also suggests that emission linewidth is affected by the particle surface chemistry and the corresponding interface with their host matrix.[52,53] It is an understatement to say the recombination of charge carriers in SiQDs is complex, since it is intimately dependent on the nanoparticle size, shape, structure, and interface.

So-called 'dangling bonds' (DBs) – unsaturated Si atoms that can act as nonradiative recombination centers for the carriers[54] – are known to adversely impact SiQD PLQY. Introduction of covalently bonded surface species (*e.g.*, alkyl, polymers, oxides, *etc*.)[42,55–63] has been met with differing degrees of success in passivating these defect states, preventing oxidation, and minimizing DB formation. Among the various approaches, alkyl-functionalized SiQDs are convenient systems for evaluating photostability because the functionalization increases solution processibility while imposing negli-

[a]*Department of Chemistry, University of Alberta, Edmonton, Alberta T6G 2G2, Canada. E-mail: jveinot@ualberta.ca*
[b]*Department of Physics, University of Alberta, Edmonton, Alberta T6G 2E1, Canada*
† Electronic supplementary information (ESI) available. See DOI: https://doi.org/10.1039/d3nr04478e

gible effects on the optical band gap of the nanoparticles.[64–66] The Kortshagan group studied 1-dodecyl functionalized SiQDs synthesized *via* plasma decomposition of silane and noted an approximate ~60% decrease in PLQY after 4 h of UV irradiation that they attributed to the formation of DBs *via* UV-induced homolytic cleavage of Si–H or Si–Si bonds.[57,58] It is well-established that amorphous silicon (a-Si) is susceptible to light-induced degradation known as the Staebler–Wronski effect (SWE) which manifests as a decrease in a-Si photoconductivity after prolonged UV light exposure.[67,68] Anthony *et al.* also observed that increasing structural disorder (*i.e.*, SiQDs with greater amorphous character) in plasma-generated SiQDs leads to decreased PLQY compared to more crystalline SiQDs.[69]

Recently, our group reported the presence of an ordered crystalline core for SiQDs with $d > 6$ nm from thermal processing of hydrogen silsesquioxane (HSQ) terminating in an amorphous 'shell'. We subsequently demonstrated that the amorphous Si (a-Si) layer can be reduced by 'over-etching' samples with ethanolic hydrofluoric acid (HF).[70,71] With the a-Si (E_g = ~1.7 eV) shell present, the particles resembled Type-I core–shell QDs due to the comparatively smaller band gap (E_g = ~1.1 eV) of the nanocrystalline Si core (nc-Si).[62,72–74] As such, the wider band gap of the a-Si is expected to provide a barrier to charge carriers (*i.e.*, holes and electrons) migrating to the particle surface resulting in less non-radiative recombination and an increased PLQY. However, questions remain: does the amorphous shell protect the SiQD core and provide access to higher PLQYs? Will the impact of the SWE on the amorphous shell result in decreased photostability and, by extension, lower PLQYs? Herein, we explore the impact of the amorphous shell on the photostability of 1-dodecyl-terminated SiQDs obtained from the reductive thermal processing of HSQ.

2. Experimental section

Reagents and materials

Sulfuric acid (reagent grade, 95–98%) was purchased from Caledon Laboratory Chemicals. Hydrofluoric acid (HF; electronics grade, 48–50%) was purchased from Fisher Scientific. Fuming sulfuric acid (reagent grade, 20% free SO_3 bases), trichlorosilane (99%), toluene (HPLC grade), methanol (reagent grade), ethanol (reagent grade), 2,2′-azobis(2-methyl propionitrile) (98%), 1-dodecene (95.0%), and benzene (anhydrous, 99.8%) were purchased from Sigma Aldrich. A PureSolv purification system equipped with N_2 as the operating gas was used for preparing dried solvents. All reagents and solvents were used as received unless otherwise specified.

Preparation of hydrogen silsesquioxane (HSQ)

HSQ was synthesized using a modified literature procedure.[75] Briefly, a mixture of concentrated (15 mL) and fuming (7 mL) sulfuric acid was prepared in a three-neck round bottom flask purged with argon and equipped with an addition funnel and Teflon coated stir bar. Dry toluene (45 mL) was then added to the acids *via* the addition funnel. A mixture of dry toluene (110 mL) and trichlorosilane (16 mL) was prepared and subsequently added dropwise into the acid-toluene mixture to obtain two-layers. The toluene layer was isolated and washed with an aqueous sulfuric acid (33% v/v) solution. The organic layer was then dried over solid $MgSO_4$ and $CaCO_3$ for 12 hours, after which the solvent volume was removed using rotary evaporation and finally dried *in vacuo* to yield a white solid.

Preparation of SiQDs/SiO_2 composite

SiQDs were prepared by way of thermally-induced disproportionation of HSQ using a well-established procedure developed in our laboratory.[76] HSQ (5 g) was placed in a standard tube furnace with a flowing 5% H_2/Ar atmosphere at 1200 or 1300 °C to yield oxide composites containing *ca.* 5 or 9 nm inclusions of elemental silicon, respectively. The composite was then mechanically ground using an agate mortar and pestle and shaken with glass beads in ethanol (~300 mL) to provide a fine powder that was used in subsequent etching procedures.

Preparation of hydride-terminated SiQDs

Hydride-terminated SiQDs (H-SiQDs) were liberated from appropriate oxide composites *via* ethanolic HF-etching of the ground composite.[71] Composite (~500 mg) obtained from processing HSQ at 1200 °C was etched using a solution (16.5 mL) of ethanol : distilled water : 49% HF (1 : 1 : 1) in a PET beaker that was equipped with a Teflon coated stir bar for a predetermined time. The liberated freestanding SiQDs were then extracted into a minimum amount of toluene (~30 mL) and collected with centrifugation before redispersing twice in toluene (~10 mL) dried over molecular sieves. These two subsequent centrifugations washes remove any residual HF. For convenience in the present discussion, we refer to "normal" H-SiQDs as those obtained from etching "1200 °C composites" for 1 h. "Over-etched" H-SiQDs were prepared similarly by etching composite (~700 mg) prepared by thermally processing HSQ at 1300 °C with a solution (24 mL) of ethanol : distilled water : HF (1 : 1 : 1) for *ca.* 3.5–4 h until the suspension colour resembles that of the 1hr etch of '1200 °C composites'. The H-SiQDs were used immediately in functionalization reactions (*vide infra*).

Preparation of dodecyl-terminated SiQDs

Radical-initiated hydrosilylation was used to functionalize the H-SiQD surfaces and render them solution processible.[64] Briefly, 'normal' H-SiQDs (~0.5 g) were dispersed in dry toluene (10 mL), 1-dodecene (6 mL), and AIBN (300 mg) in an Ar-purged Schlenk flask equipped with a Teflon coated stir bar. The reaction mixture was subsequently degassed *via* three sequential freeze–pump–thaw cycles and placed in an oil bath at 70 °C for 17–19 h under flowing Ar. After cooling to room temperature, surface functionalized SiQDs isolated from the reaction mixture *via* centrifugation with toluene and methanol. 'Over-etched' H-SiQDs (~0.7 g) were functionalized using the same procedure in dry toluene (14 mL) and 1-dodecene

(8.4 mL) with an AIBN (420 mg) initiator. After purification, the wet pellets of SiQDs were dispersed in a minimum amount of benzene (*ca.* 1 mL), filtered using a 0.45 μm PTFE syringe filter into a pre-weighted vial, and freeze-dried. Solid dodecyl-SiQDs were massed in the vial, transferred into the glovebox, redispersed with dry toluene (~2 mg ml^{-1}), and stored in subdued light until needed.

Photodegradation of dodecyl-terminated SiQDs suspensions

Photodegradation experiments were performed using a custom the Schlenk flask equipped with a quartz insert to facilitate exposure to the emission from a UV light LED source (365 nm, Nichia, model NCSU033A operated at 4.5 V). In an Ar-filled glovebox, the toluene suspension of functionalized SiQDs (*i.e.*, normal or over-etched) was transferred to the Schlenk flask that was already equipped with a pre-dried Teflon stir bar and the quartz insert was affixed. The sealed flask containing the SiQD suspension was then removed from the glovebox and affixed to a standard Schlenk manifold with Ar working gas. The flask was wrapped with aluminum foil and irradiation commenced under flowing Ar while the apparatus was maintained at 10 °C. Aliquots were taken at predefined time intervals using a glass syringe and stored in the glovebox until needed for analyses.

Optical characterization

Optical characterization of all SiQD suspensions was performed in a quartz cuvette (1 cm × 1 cm). Photoluminescence (PL) spectra were acquired by exciting samples using the combined 351 and 364 nm lines of an argon ion laser and collecting the emission using an optic fiber connected to an Ocean Optics USB 2000+ Spectrometer. A 425 nm long-pass filter (LPF) was used to eliminate scattered light from the excitation source. The spectral response was calibrated using a blackbody radiator. Time-resolved PL (PL lifetime) measurements were acquired using the same laser (20 mW) interfaced to an acoustic-optic modulator (50 ns response time) operated at a frequency of 100 Hz with a 50% duty cycle. The PL was captured by an optic fiber, sent through a 500 nm long-pass filer, and counted by a Hamamatsu H7422P-50 photomultiplier tube (PMT) interfaced with a Becker-Hickl PMS-400A gated photon counter. The data was collected without wavelength selection and used 1 μs time steps. The mean PL decay lifetimes were found by fitting the data using a log–normal lifetime distribution function.[51,77] UV-vis absorption spectra were measured using the Ocean Optics USB 2000+ spectrometer with a MINI-D2T Deuterium Tungsten light source (λ_{ex} = 200–1000 nm).

Absolute PL quantum yield (PLQY) measurements were performed using an integrating sphere with a 365 nm light-emitting diode excitation source. Solutions were diluted to have an absorbance between 0.08 to 0.13 at 400 nm. The PL and excitation intensities were measured through an optical fiber and analyzed with an Ocean Optics 2000+ spectrometer using a NIST-calibrated light source for absolute irradiance measurements. The measurements were done in triplicate.

Fourier transform infrared spectroscopy (FT-IR)

SiQDs were drop-cast onto a silicon wafer from dry toluene suspensions and the toluene was evaporated under ambient conditions. FT-IR spectra were acquired using a Thermo Nicolet 8700 FTIR Spectrometer equipped with a microscope.

X-ray photoelectron spectroscopy (XPS)

Samples were prepared by drop-casting toluene suspensions of SiQDs onto copper foil. XP spectra were measured using Kratos Axis 165 Ultra X-ray photoelectron spectrometer with a monochromatic Al Kα source operating at 210 W with an energy $\hbar\nu$ = 1486.6 eV. Survey spectra were acquired using an analyzer pass energy of 160 eV and a step size of 0.3 eV. For high-resolution spectra, a pass energy of 20 eV and a step size of 0.1 eV were used. All spectra were calibrated to C 1s (284.4 eV) using CasaXPS (VAMAS) software with a Shirley-type background to remove most of the extrinsic loss structure. The Si 2p region was fit to appropriate spin–orbit splitting with Si $2p_{3/2}$ and Si $2p_{1/2}$ components – the doublet area ratio fixed at 2 : 1 and separated spin–orbit splitting fixed at 0.62 eV.

Thermal gravimetric analysis (TGA)

Dried SiQDs were transferred to an appropriate platinum pan that was placed in a Mettler Toledo TGA/DSC 1 star system. The sample weight loss was monitored in a N_2 atmosphere over the temperature range of 25 to 700 °C at a temperature ramp rate of 10 °C min^{-1}. Estimation of ligand surface coverage was determined using an established literature procedure.[15]

X-ray diffraction (XRD)

XRD samples were prepared by drop-casting toluene suspensions of SiQDs onto a zero-background Si wafer and measured in a thin film orientation using a Rigaku Ultima IV multipurpose X-ray diffraction system equipped with a Cu Kα source. For thin-film diffraction, a parallel beam was used with a glancing angle of 0.5°. The XRD peaks were analyzed with the Debye-Scherrer equation: $d_{xrd} = \frac{K\lambda}{\beta\cos\theta}$, where d_{xrd} is the mean size of the crystalline domain, K is the shape factor (K = 0.94 for spherical crystals with cubic lattice),[78] λ is the X-ray wavelength ($\lambda_{CuK\alpha}$ = 0.15406 nm), β is the full-width-at-half-maximum (FWHM) of the reflections (rad), and θ is the Bragg angle (rad).

Raman spectroscopy

Samples were prepared by drop-casting toluene suspensions of SiQDs onto a copper foil. Spectra were acquired using a Renishaw Raman microscope InVia upon excitation with a 532 nm laser.

Electron paramagnetic resonance (EPR)

EPR samples were prepared in EPR tubes containing a capillary tube with SiQDs toluene suspension (0.2 mL) inside a nitrogen-filled glovebox. The EPR tubes were capped and sealed with Parafilm to minimize exposure to ambient atmo-

sphere throughout the EPR measurement. Spectra were acquired on a Bruker EMX Nano spectrometer at room temperature with X-band microwave (applied frequency of 9.636859 GHz) and a microwave attenuation of 25 dB. The field was centered at 3434 G with a sweep width of 500 G and sweep time of 75 s. A receiver gain of 30 dB and modulated amplitude of 5 G were set. Each spectrum was measured with 2 scans.

Transmission electron microscopy (TEM)

TEM samples were prepared by depositing a drop of a dilute toluene suspension of the sample in question onto a holey or ultra-thin carbon-coated copper grid (obtained from Electron Microscopy Inc.). The grid bearing the sample was subsequently transferred to a vacuum chamber at a base pressure of 0.2 bar for at least 24 h prior to data collection. Bright field TEM images were acquired using a JEOL JEM-ARM200CF S/TEM electron microscope with an accelerating voltage of 200 kV. High-resolution (HR) TEM images were processed using Gatan Digital Micrograph software (Version 3.4.1).

3. Results and discussion

'Normal' (N) SiQDs bearing thick a-Si shell and 'over-etched' (O) SiQDs with thin-to-no amorphous layer were subjected to the emission from a 365 nm UV lamp for up to 72 h. The integrity of the SiQDs was evaluated using optical, structural, and compositional analyses before and after exposure. To interrogate the impact of an a-Si shell on the photostability of SiQD optical properties, it was necessary to prepare nanoparticles with the same physical dimensions but different crystallinity (*i.e.*, crystalline core/a-Si shell *vs.* crystalline). To realize these SiQD classes, we thermally processed HSQ at 1200 and 1300 °C in a slightly reducing atmosphere to yield different oxide composites containing elemental silicon inclusions with dimensions of *ca.* 5 and *ca.* 9 nm, respectively (Scheme 1). SiQDs were then liberated from the protective silicon oxide matrix *via* alcoholic HF etching. Materials prepared in this way comprise a crystalline core and amorphous shell; the majority of the a-Si shell can then be removed with prolonged HF etching.[71] For ease of understanding, our present discussion refers to the SiQDs bearing a thicker amorphous shell obtained from the 1200 °C-processed composite and subjected to aqueous ethanolic HF etching for 1 h as 'normal'. 'Over-etched' SiQDs were prepared by prolonged etching (*i.e.*, 3.5–4 h) of the composite processed at 1300 °C. The extended etching simultaneously removes the thick amorphous shell and reduces particle dimensions to align closely with those of the N-SiQDs. Following liberation from the oxide, both classes of SiQDs were surface modified with 1-dodecene *via* AIBN-initiated radically-induced hydrosilylation to yield solution-stable dodecyl-SiQDs. Four batches of N-SiQDs and five batches of over-etched O-SiQDs were prepared.

Representative bright-field TEM images (Fig. 1a and c) indicate that dodecyl functionalized N-SiQDs and O-SiQDs possessed statistically identical physical dimensions of 5.1 ± 1.2 nm (Fig. 1b) and 5.3 ± 1.1 nm (Fig. 1d), respectively. As expected, corresponding dark-field TEM images (Fig. S1†) also revealed equivalent sizes. In contrast to our TEM analysis, Debye-Scherrer fit of the XRD patterns (Fig. 1e) indicates N-SiQDs possess an XRD crystallite size of *ca.* 3.5 nm while O-SiQDs exhibit an average XRD crystallite size of *ca.* 4.9 nm. This observation is expected and consistent with previous studies.[71] Raman spectroscopy was used to probe the order/disorder structures present in the nanoparticles. Fig. 1f shows the Raman spectra of both SiQD classes comprising a sharp peak at *ca.* 512 cm^{-1} that is attributed to nanocrystalline Si (nc-Si).[79,80] In contrast to the single, asymmetric Lorentzian peak observed for O-SiQDs, a broad shoulder at approximately 470 cm^{-1} is also evident in the spectrum of the N-SiQDs that arises from a-Si.[81] The combined TEM, XRD, and Raman analyses, as well as our previous report,[70] all point to over-etching being effective in the removal of the amorphous shell from O-SiQDs. FT-IR and XP (Fig. S2†) spectra were measured and suggest the two sets of nanoparticles were of equivalent composition. In addition, a weight loss of *ca.* 45% noted in TGA (Fig. S2†) for both sets of SiQDs further suggesting a similar degree of surface functionalization (*i.e.*, *ca.* 55%).

The PL of the as-produced SiQDs is summarized in Table S1† and compared using boxplots (see Fig. 2). Both

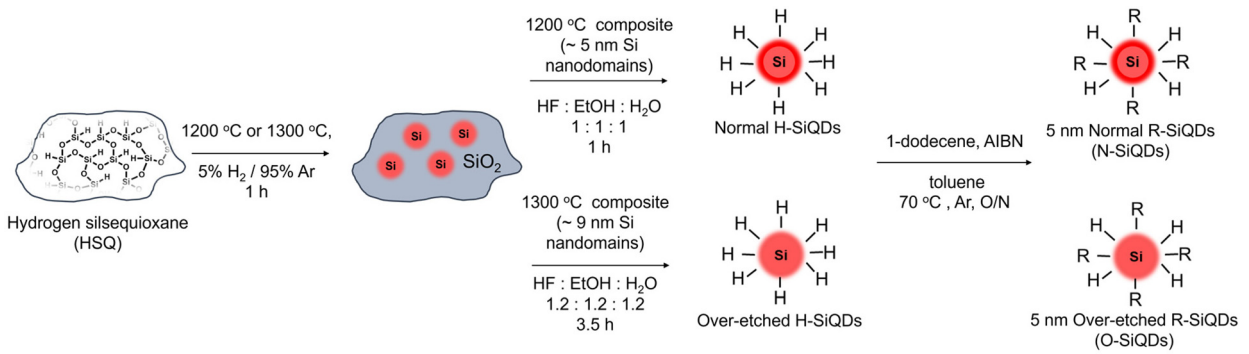

Scheme 1 Preparation of 'normal' and 'over-etched' dodecyl-functionalized SiQDs. Freestanding H-SiQDs were liberated from HF-etching of thermally-processed HSQ, followed by radical-initiated hydrosilylation with 1-dodecene.

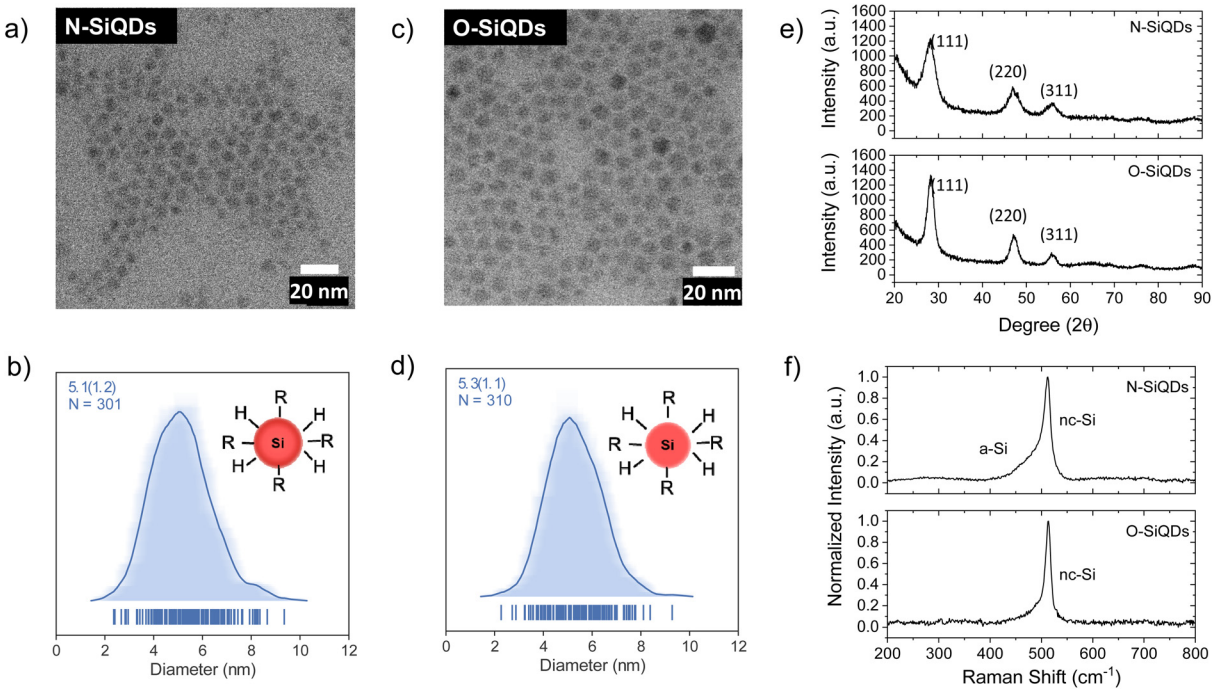

Fig. 1 Structural characterization of the SiQDs used in this study. Brightfield TEM images show equivalent physical dimensions of (a) N-SiQDs (5.1 ± 1.2 nm) and (c) O-SiQDs (5.3 ± 1.1 nm). The respective size distributions, (b) and (d), are presented as average-shifted histograms. (e) XRD patterns, and (f) Raman spectra show evidence of greater long-range order in O-SiQDs.

N- and O-SiQDs exhibited featureless UV-vis absorption spectra (Table S1†). The QDs all emitted near-infrared PL centered in the range of 810 to 940 nm with broad emission bandwidths (full-width-at-half-maximum (FWHM) in the range of *ca.* 129 to 234 nm; Fig. S3 and S4†). Characteristic S-band Si PL lifetimes of 160 to 400 μs were also observed for both classes of QDs.[82] O-SiQDs exhibited similar mean PL maxima and longer mean PL lifetime than the N-SiQDs; however, no statistical differences in these properties were found between the two classes of samples (Fig. 2a and b).

PLQY of the as-produced SiQDs were measured to establish whether the inclusion of an a-Si shell influences the radiative recombination of excitons. Recall, PLQY quantifies the efficiency of QDs in producing emitted photons from absorbed photons and depends upon the specific radiative and all non-radiative processes as summarized in eqn (1) and (2):

$$\mathrm{PLQY}\,(\eta) = \frac{\text{photons emitted}}{\text{photons absorbed}} = \frac{k_r}{k_r + \sum k_{nr}} \quad (1)$$

where k_r is radiative recombination rate (μs^{-1}) and k_{nr} is non-radiative recombination rate (μs^{-1}). Expressed in terms of the lifetimes,

$$\mathrm{PLQY}\,(\eta) = \frac{\tau_{pl}}{\tau_r} = \frac{(\tau_r + \tau_{nr})}{\tau_r} \quad (2)$$

where τ_{pl} is photoluminescence lifetime (μs), τ_r is radiative recombination lifetime, and τ_{nr} is non-radiative recombination lifetime.[83] The PLQY of the batches of as-produced N-SiQDs was in the range of 24 to 41%, meanwhile the PLQY of O-SiQD batches ranged between 19 to 38% (Fig. 2c). The respective radiative recombination rate ratio (k_r/k_{nr}) ranged between 0.25 to 0.69 (Fig. 2d). Interestingly, a narrower distribution of PLQY and k_r/k_{nr} was observed from O-SiQDs. The mean PLQY and k_r/k_{nr} of N-SiQDs are higher than that of O-SiQDs, yet the difference is not statistically significant.

The bulk band gap of a-Si is larger than that of bulk crystalline silicon (*e.g.*, *ca.* 1.7 eV[73] *vs. ca.* 1.1 eV[74]). An a-Si shell hence is expected to provide a passivation layer that would confine photo-excited charge carriers to the crystalline core and limit surface state-related non-radiative recombination pathways directly analogous to what is observed from traditional Type-I QDs. However, we note that N-SiQDs have similar PLQY as the O-SiQDs. One must consider that a 1 to 3 nm thick a-Si layer can have a varying number of trap states in the band gap which could lead to electron–hole delocalization at the a-Si : c-Si interface.[84] We hypothesize that the positive effects of the large band gap a-Si shell are counteracted by the negative effects of defects introduced by the amorphous structure. The balanced effect therefore showed minimal improvement in the radiative recombination in N-SiQDs. The removal of this a-Si shell, which comes with the loss of corresponding trap states, could lead to the narrower spread of radiation recombination rates observed for O-SiQDs (*vide supra*). A detailed investigation of the relationship between the thickness and quality of the amorphous layer on the optical pro-

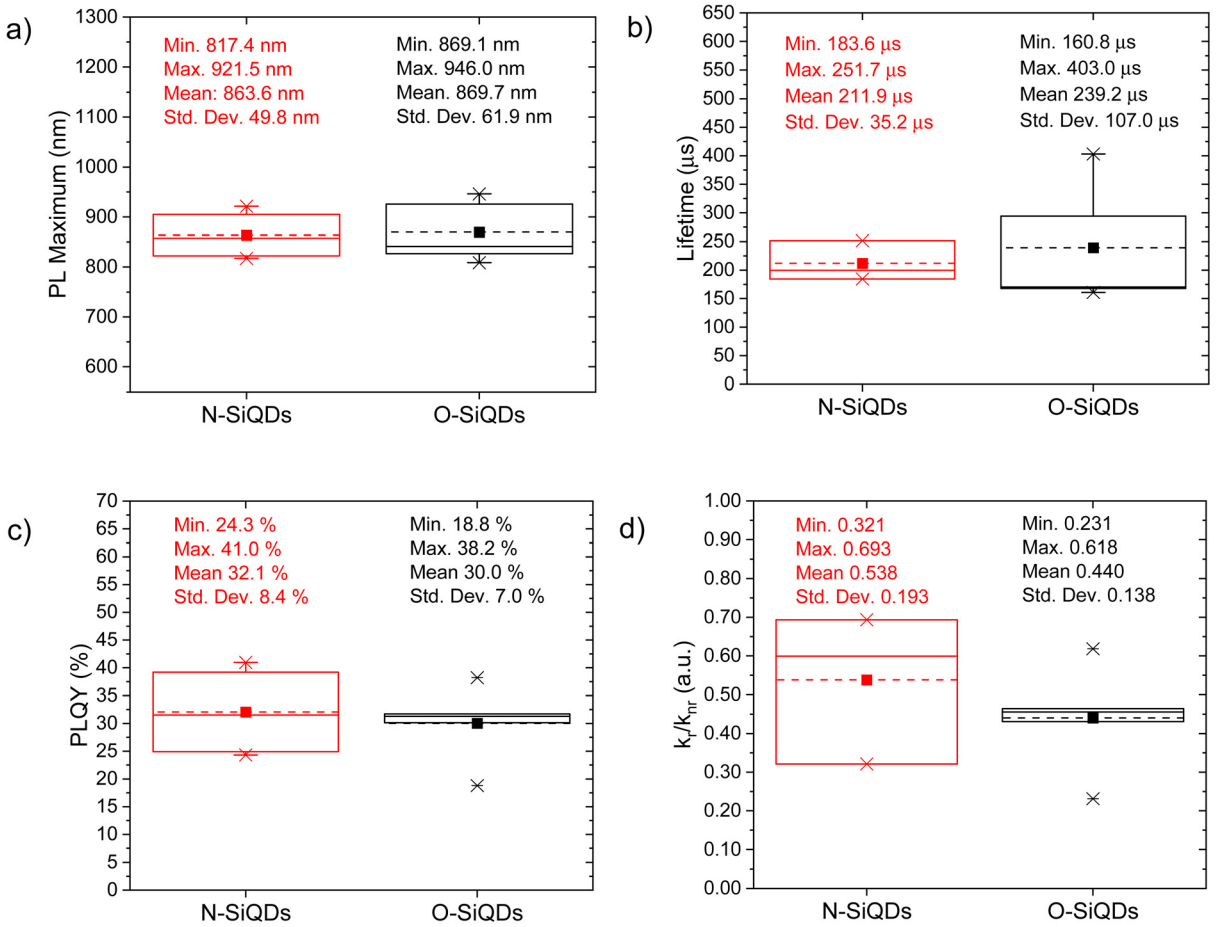

Fig. 2 Boxplots comparing the (a) PL max, (b) mean PL lifetime, (c) PLQY, and (d) k_r/k_{nr} of the as-produced N-SiQDs an5555d O-SiQDs. Mean and median of the distributions are represented by dash and solid lines in the boxes, respectively.

perties of the nanoparticles would be of interest to uncover the potential of core–shell structure, however precise control on tuning of the amorphous shell is yet to be explored and is beyond the scope of this study.

To study the photostability of N-SiQDs and O-SiQDs, the materials were suspended in dry toluene and irradiated by 365 nm UV-LEDs at 4.5 V under an Ar atmosphere for 72 h. Aliquots were extracted at predefined time intervals and evaluated by PL, UV-vis absorption, emission lifetime, and PLQY as summarized in Fig. 3. A small shift in PL maximum (<10 nm; Fig. 3a) was occasionally observed that we attribute to trace oxidation occurring during material handling and data acquisition (Fig. S3 and S4†). Of important note, these shifts were negligible compared to previously reported prominent oxidation-induced blue-shift.[51,85]

The decrease of the PLQY observed for the SiQD suspensions results primarily from the influence of surface defects and/or DBs created as a result of UV irradiation. On average, both classes of SiQDs maintained *ca.* 90% of their initial PLQYs (Fig. 3b and Tables S2, S3†) during the first 24 h of irradiation. After which, the average PLQY of N-SiQDs continued to decrease to *ca.* 80% of its original value after 48 h irradiation and finally to *ca.* 70% after 72 h. O-SiQDs maintained *ca.* 90% of their initial PLQY for the first 48 h before eventually decreasing to *ca.* 70% after 72 h. A similar photostability study by Wu *et al.* observed a plateau in PLQY loss after reaching *ca.* 20% in SiQDs that were synthesized using non-thermal plasma methods.[58] It is unclear if these particles possess an a-Si shell. Regardless, both studies suggest dodecyl-SiQDs reach a steady state of *ca.* 20–30% decrease from their "as prepared" original PLQY following prolonged UV irradiation. Although the quantum efficiency decreased as a result of irradiation, the PL lifetimes remained fairly consistent (Fig. 3c). Using eqn (1) and (2), the radiative and non-radiative decay rates can be determined independently (Fig. 3d). The trends of recombination rates are fitted with a linear regression (Fig. S5 and Table S4†). In general, for N-SiQDs with amorphous shells, the non-radiative rate increased with a decrease in radiative rate upon irradiation; whereas for the O-SiQDs the radiative and non-radiative rates remained constant. These observations further point to the reduced optical stability of N-SiQDs.

We hypothesize that these observations can be understood in the context of the Staebler–Wronski effect, in which

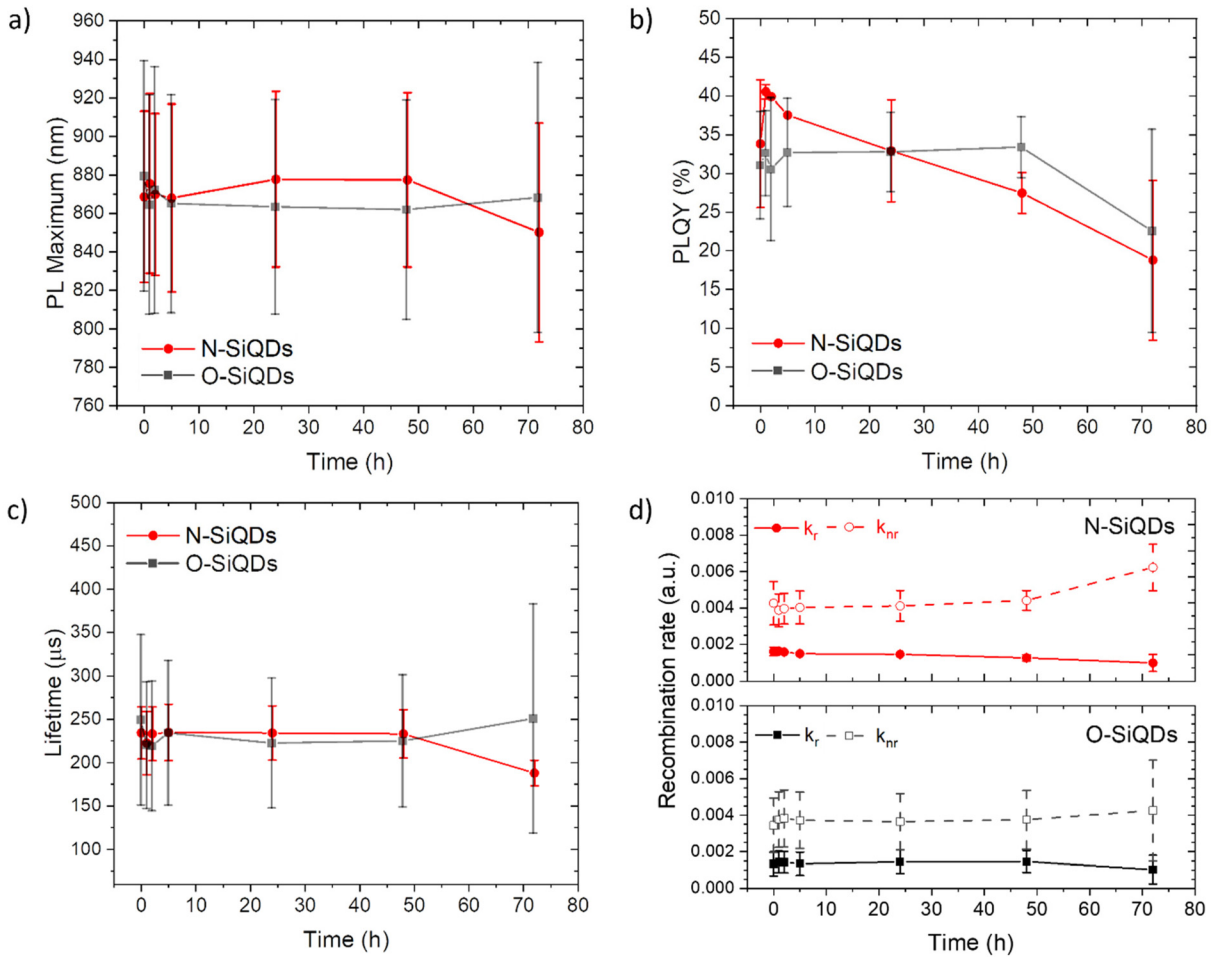

Fig. 3 A summary of the optical properties of N-SiQDs (red circles) and O-SiQDs (black squares). (a) PL maxima, (b) PLQY, (c) PL lifetime, and (d) recombination rate ratio as a function of time over a period of 72 h of UV irradiation. Error bars represent the 95% limit of measurement. Representative PL and UV-vis absorption spectra of each sample are plotted in Fig. S3, S4 and summarized in Tables S2, S3.†

irradiation of a-Si could generate dangling bonds that reduce radiative recombination. A recent STM study reported by Kislitsyn *et al.* provides a more direct visualization of a-Si generating dangling bonds and deep charge traps by applying electrons to the amorphous shell of SiQDs through the STM tip.[81] In addition to the defects formed at the surface of a-Si, the formation of dangling bonds at the amorphous-Si : crystalline-Si interface (a-Si : c-Si) could also lead to a decrease in radiative recombination efficiency. Plagwitz *et al.* similarly attributed an increase in the surface recombination velocity to defects at the a-Si : c-Si interface.[68] A potential mechanism for decreased k_r involves charge carrier tunneling from the QD core to the interface, where the charge carriers non-radiatively recombine. In contrast, O-SiQDs exhibit minimal changes in recombination rate under similar conditions; this underscores the unique role of the a-Si shell in modulating radiative recombination dynamics during prolonged illumination.[86] Nevertheless, it is important to note that the slope is two to three orders of magnitude (10^{-5} to 10^{-6}) smaller than the k values (10^{-3}) and the sample size of N-SiQDs is smaller than O-SiQDs. Studies that are beyond the scope of the present paper are ongoing to explore the origin of the decrease. A prospective transient absorption and scanning tunneling spectroscopic[81,87,88] study provided insights into the photophysics and electronics of the different SiQDs under illumination.

The creation of dangling bonds through Si–H and Si–Si cleavage will certainly lead to a decrease in PL and conductivity and result in surface species desorption from the nanoparticles in the form of $^{\bullet}SiH_{3(g)}$ and $^{\bullet}H_{(g)}$.[89,90] To account for this, samples of SiQDs with and without 72 h of irradiation were characterized by XPS and FT-IR to probe any changes in their structure and compositions. As expected, XP spectra of the SiQDs were the same (Fig. S5†) showing similar Si species regardless of the degradation, suggesting minimal oxidation. Likewise, both classes of SiQDs show comparable features in their FT-IR spectra, aside from a minor increase in the Si-O_x stretches at ~1100 cm^{-1} caused by exposure to oxygen during the measurement (Fig. S6†).

The Si-H_x stretching features in FT-IR spectra (Fig. 4) can be readily deconvoluted into ≡SiH (ν = 2075 cm^{-1}), =SiH_2 (ν =

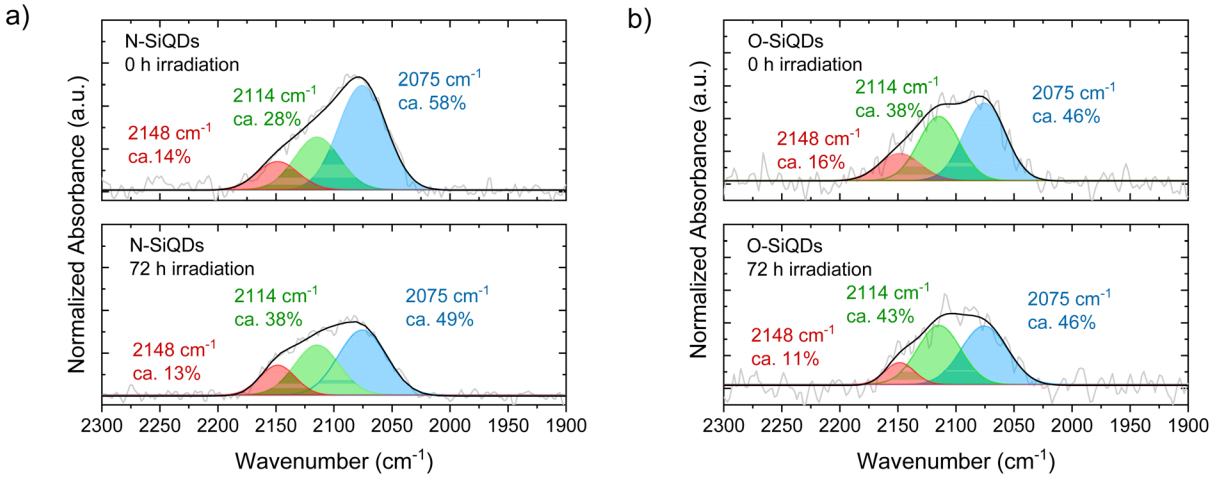

Fig. 4 Deconvoluted FT-IR spectra of (a) N-SiQDs and (b) O-SiQDs as prepared (top) and following 72 h UV irradiation (bottom) spanning the SiH_x stretching region and deconvoluted to show the contributions from SiH_3 (red), SiH_2 (green), and SiH (blue) components. In general, a decrease in the SiH_3 contribution is noted after irradiation.

2114 cm^{-1}), and $-SiH_3$ (ν = 2148 cm^{-1}) to probe potential surface changes induced by expires to 365 nm UV ($E_{h\nu}$ = 3.4 eV) irradiation.[85,91] The as prepared samples that were not exposed to UV irradiation show ≡SiH being the dominant surface species followed by $=SiH_2$, and $-SiH_3$ with a peak area ratio of ≡SiH : $=SiH_2$: $-SiH_3$ is 58 : 28 : 14 and 46 : 38 : 16 for N- and O-SiQDs, respectively. The different ratios of the SiH_x species may be attributed to changes in the QD surface morphology upon removal of a-Si shell. The impact of extended HF etching on the surface species is, however, beyond the scope of the study and remains the subject of ongoing investigations. Upon UV exposure, *ca.* 20% and 6% decrease in Si–H_x stretches are observed for N-SiQDs and O-SiQDs, respectively. This observation is expected as the irradiation can cleave bonds within the SiQDs as summarized in Fig. 5. The deconvoluted FT-IR spectra after irradiation reveal a decrease in the intensity of features associated with $-SiH_3$ and ≡SiH and an increase in those associated with $=SiH_2$. The reduction in the $-SiH_3$ abundance (11% for N-SiQDs and 33% for O-SiQDs) is frequently attributed to $^{\bullet}SiH_3$(g) desorption from homolytic cleavage of Si–SiH_3 (B.E. ~2.0–2.7 eV).[90,92,93] The H–Si bond of $=SiH_2$ (B.E. ~3.2 eV) on the strained SiQD surface is also susceptible to bond cleavage that yields $^{\bullet}H_{(g)}$ and $^{\bullet}SiH_{(s)}$.[89,94,95] Comparatively, the ≡SiH silane bond should be most stable with a B.E. of ~3.6 eV.[89] The decrease in the concentration of monohydrides (*i.e.*, ≡SiH) and increase dihydrides (*i.e.*, $=SiH_2$) seem to contradict the relative stabilities estimated from their bond strength but, nonetheless, they can be understood in the context of the complex surface structure of the nanoparticles. While a bulk silicon surface comprises specific crystal planes (*e.g.*, Si(100) containing $=SiH_2$; Si(111) containing ≡SiH), the present small SiQDs do not have well-defined facets.[96–98] The silicon hydrides on the nanoparticles cannot be said to reside on ordered planes, rather, they are located on a small crystal terraces with numerous steps and edges. Upon release of volatile $^{\bullet}SiH_{3(g)}$ and $^{\bullet}H_{(g)}$, it is reasonable that the liberated species could further react with neighboring silicon hydrides, resulting in silanes ($SiH_{x(g)}$) and hydrogen gas ($H_{2(g)}$).[90,99,100] This complex structure together with the reactive radicals could enable $=SiH_2$ formation in expense of normally less reactive ≡SiH. The consistent loss of $-SiH_3$ components suggests surface species desorption resulted from SiQDs photodegradation.

The size and shape of the SiQDs after UV irradiation were evaluated by TEM. The corresponding microscopy images (bright-field Fig. 6a and b and dark-field Fig. S7a and b†) revealed the preservation of the spheroidal shapes in both sets of nanoparticles. The size distributions of the corresponding images (Fig. 6c, d and Fig.S7c, d†) indicated a 2% shrinkage in N-SiQDs and a 4% decrease in O-SiQDs consistent with surface

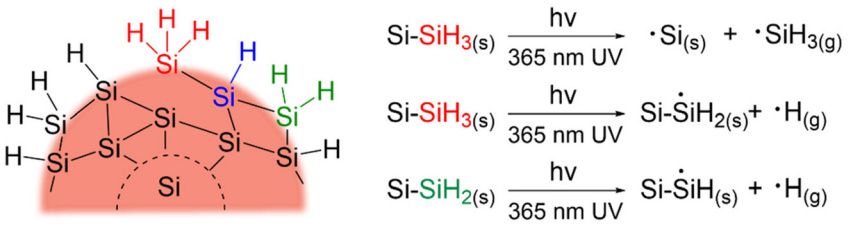

Fig. 5 Summary of possible bond breakages in SiQDs upon 365 nm UV irradiation.

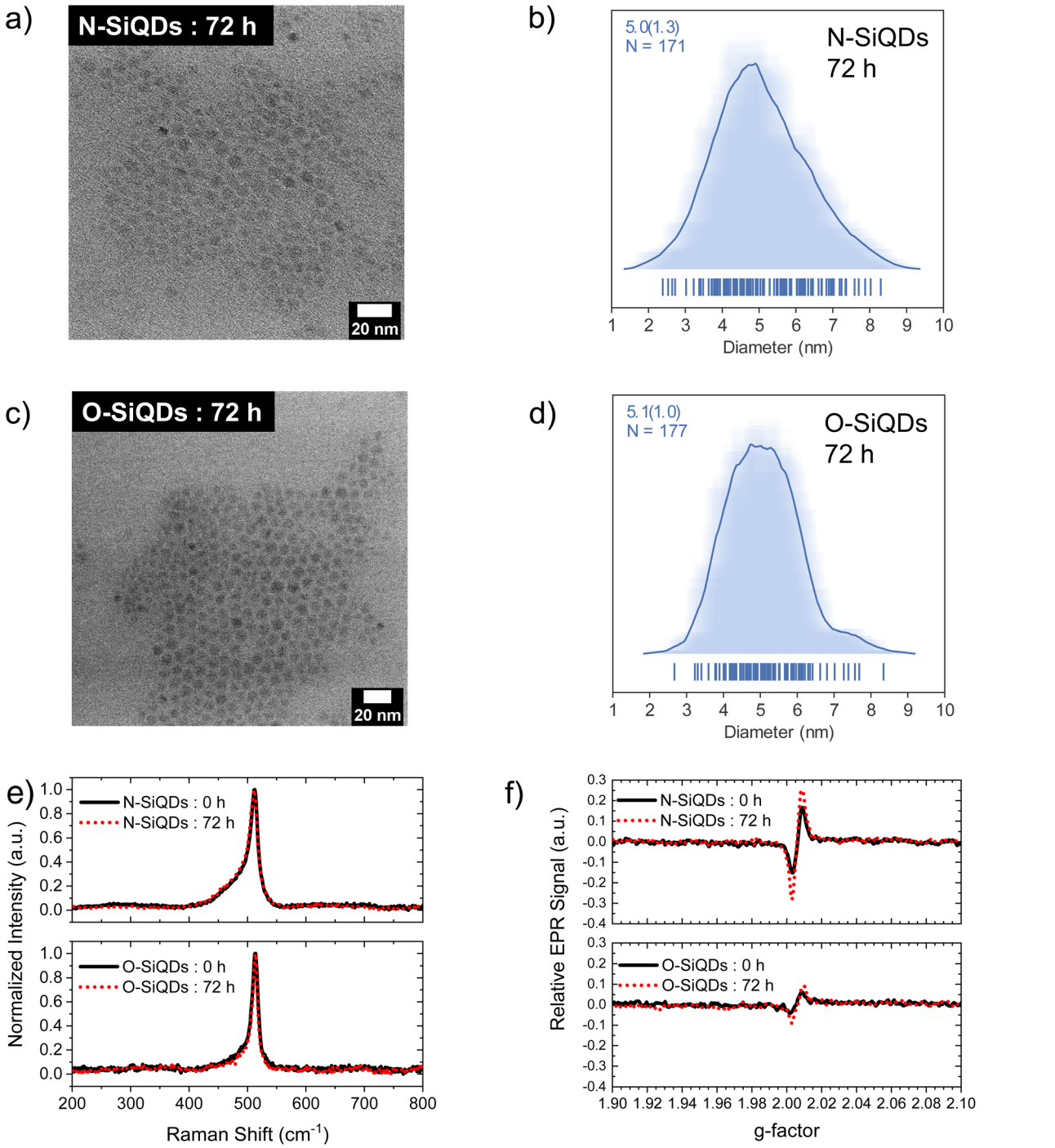

Fig. 6 Bright-field TEM images showing equivalent physical sizes of (a) N-SiQDs and (b) O-SiQDs. The respective size distributions, (c) and (d), were plotted as average-shifted histograms. (e) Raman spectra and (f) EPR signals comparing N-SiQDs and O-SiQDs before and after 72 h of irradiation. Black solid lines and red dotted lines indicate data obtained from nanoparticles before and after irradiation, respectively.

atom desorption. However, it is important to note that these changes are within the error of the method and should not be over emphasized. Similarly, the Raman spectra (Fig. 6e) of the irradiated particles similarly remain unchanged from the as-produced nanoparticles. An investigation using *in situ* TEM[101] and solid-state NMR[102] could potentially provide additional insight into these structural changes and deepen our understanding of the evolving SiQD surface, however such studies are outside the current capability of our instrumentation.

With the knowledge that the instability of radiative recombination in SiQDs is a result of the generation of defects at the nanoparticle surfaces, EPR spectroscopy was used to assess

the relative densities of unpaired electron spins in the two sets of SiQDs. Toluene solutions of as-prepared and 72-hour-irradiated SiQDs (2 mg mL^{-1}) were evaluated (Fig. 3b). For both systems, the EPR signal appeared in the range of *g*-factor 2.00 to 2.01 and can be ascribed to dangling bonds on silicon in a disordered environment (g_D at ~2.005) and asymmetric P_b centers at the interface of the Si nanocrystal and its oxide shell ($g_\perp$ at ~2.008 and $g_\parallel$ at ~2.002).[80,103] The EPR signal from N-SiQDs was qualitatively more than twice as intense as that from O-SiQDs before and after irradiation; this observation is consistent with our observations of decreased PLQY and k_r/k_{nr} values. Considering the two sets of nanoparticles had a similar degree of alkyl passivation, the more intense EPR signals of N-SiQDs can reasonably be ascribed to a greater number defects at the a-Si surface and a more disordered Si : SiO_x and a-Si : nc-Si interface. This observation aligns with a density functional theory (DFT) study by Bushlanova *et al.*, which indicated that amorphous Si_nH_{2m} nanoclusters with sizes of ~1 nm contained dangling bonds at the cluster surface in comparison to their crystalline counterpart.[104] Prospective *in situ* characterization, pump–probe spectroscopy, and STM measurements would be essential to further understand the photophysics and degradation mechanisms between the different nanoparticles and are the subject of future work.

4. Conclusions

In this study, *ca.* 5 nm dodecyl-functionalized silicon quantum dots, with (N-SiQDs) and without (O-SiQDs) 'thick' amorphous shells, were prepared. The presence of amorphous layer did not significantly affect the optical properties (*i.e.*, photoluminescence maxima, lifetime, and photoluminescence yield) of the as-produced nanoparticles. However, the quantum yield of N-SiQDs was less stable to prolonged UV irradiation compared to O-SiQDs. Structural analyses presented here indicate the adverse effects of the amorphous shell can be reasonably attributed to the generation of defects in the disordered SiQD structure. Our study provides valuable insight into the stability of SiQDs and will enable a better understanding of their core–shell structure with the target of stable luminescent systems.

Author contributions

Cheong, I. T. was responsible for experimental design, SiQDs synthesis, PL degradation experiments, data collection and analysis, and manuscript preparation. Yang Szepesvari L. assisted with SiQDs synthesis, conducting PL degradation experiments, and PLQY data collection. Ni C. collected the TEM images. Butler C. acquired the XP spectra. O'Connor, K. M. assisted with HF etching training and manuscript editing. Hooper R. assisted with EPR acquisition and manuscript editing. Meldrum, A. assisted with data interpretation and manuscript edits. Veinot, J. G. C. was the supervisory author.

Conflicts of interest

There are no conflicts to declare.

Acknowledgements

The authors acknowledge the continued generous funding from the ATUMS training program supported by NSERC CREATE (CREATE-463990-2015), the Natural Science and Engineering Research Council (NSERC Discovery Grant program; RGPIN-2015-03896), Alberta Innovates Strategic Projects program, as well as Future Energy System (FES) which is supported by the Canada First Research Excellence Fund (CFREF). Finally, we thank the efforts of all the staff and other authors who have contributed to this work.

References

1 G. Ledoux, J. Gong, F. Huisken, O. Guillois and C. Reynaud, *Appl. Phys. Lett.*, 2002, **80**, 4834–4836.
2 R. J. Clark, M. K. Dang and J. G. Veinot, *Langmuir*, 2010, **26**, 15657–15664.
3 C. M. Hessel, D. Reid, M. G. Panthani, M. R. Rasch, B. W. Goodfellow, J. Wei, H. Fujii, V. Akhavan and B. A. Korgel, *Chem. Mater.*, 2012, **24**, 393–401.
4 M. Dasog, G. B. De los Reyes, L. V. Titova, F. A. Hegmann and J. G. C. Veinot, *ACS Nano*, 2014, **8**, 9636–9648.
5 S. Ivanov, S. Zhuravsky, G. Yukina, V. Tomson, D. Korolev and M. Galagudza, *Materials*, 2012, **5**, 1873–1889.
6 A. Das and P. T. Snee, *ChemPhysChem*, 2016, **17**, 598–617.
7 A. Shiohara, S. Hanada, S. Prabakar, K. Fujioka, T. H. Lim, K. Yamamoto, P. T. Northcote and R. D. Tilley, *J. Am. Chem. Soc.*, 2010, **132**, 248–253.
8 U.S. Department of Health and Human Services, Toxicity and Carcinogensis Studies of Indium Phosphide, 2001.
9 R. Hardman, *Environ. Health Perspect.*, 2006, **114**, 165–172.
10 J. Sobhanan, J. V. Rival, A. Anas, E. Sidharth Shibu, Y. Takano and V. Biju, *Adv. Drug Delivery Rev.*, 2023, **197**, 114830.
11 K. Y. Cheng, R. Anthony, U. R. Kortshagen and R. J. Holmes, *Nano Lett.*, 2011, **11**, 1952–1956.
12 B. Ghosh, Y. Masuda, Y. Wakayama, Y. Imanaka, J.-I. Inoue, K. Hashi, K. Deguchi, H. Yamada, Y. Sakka, S. Ohki, T. Shimizu and N. Shirahata, *Adv. Funct. Mater.*, 2014, **24**, 7151–7160.
13 J. Watanabe, H. Yamada, H.-T. Sun, T. Moronaga, Y. Ishii and N. Shirahata, *ACS Appl. Nano Mater.*, 2021, **4**, 11651–11660.
14 Y. C. Zhang, Z. Y. Yu, X. Y. Xue, F. L. Wang, S. Li, X. Y. Dai, L. Wu, S. Y. Zhang, S. Y. Wang and M. Lu, *Opt. Express*, 2021, **29**, 34126–34134.
15 I. T. Cheong, J. Mock, M. Kallergi, E. Groß, A. Meldrum, B. Rieger, M. Becherer and J. G. C. Veinot, *Adv. Opt. Mater.*, 2022, **11**, 2201834.

16 F. Meinardi, S. Ehrenberg, L. Dhamo, F. Carulli, M. Mauri, F. Bruni, R. Simonutti, U. Kortshagen and S. Brovelli, *Nat. Photonics*, 2017, **11**, 177–185.
17 R. Mazzaro, A. Gradone, S. Angeloni, G. Morselli, P. G. Cozzi, F. Romano, A. Vomiero and P. Ceroni, *ACS Photonics*, 2019, **6**, 2303–2311.
18 S. Han, G. Chen, C. Shou, H. Peng, S. Jin and C.-C. Tu, *ACS Appl. Mater. Interfaces*, 2020, **12**, 43771–43777.
19 J. Huang, J. Zhou, E. Jungstedt, A. Samanta, J. Linnros, L. A. Berglund and I. Sychugov, *ACS Photonics*, 2022, **9**, 2499–2509.
20 T. Lin, X. Liu, B. Zhou, Z. Zhan, A. N. Cartwright and M. T. Swihart, *Adv. Funct. Mater.*, 2014, **24**, 6016–6022.
21 M. Dutta, L. Thirugnanam, P. V. Trinh and N. Fukata, *ACS Nano*, 2015, **9**, 6891–6899.
22 E. J. Henderson, A. J. Shuhendler, P. Prasad, V. Baumann, F. Maier-Flaig, D. O. Faulkner, U. Lemmer, X. Y. Wu and G. A. Ozin, *Small*, 2011, **7**, 2507–2516.
23 C. J. T. Robidillo, M. A. Islam, M. Aghajamali, A. Faramus, R. Sinelnikov, X. Zhang, J. Boekhoven and J. G. C. Veinot, *Langmuir*, 2018, **34**, 6556–6569.
24 Z. F. Li and E. Ruckenstein, *Nano Lett.*, 2004, **4**, 1463–1467.
25 D. Yang, Z. Cui, Z. Wen, Z. Piao, H. He, X. Wei, L. Wang, S. Mei, W. Zhang and R. Guo, *ACS Mater. Lett.*, 2023, **5**, 985–1008.
26 Z. Kang, C. H. A. Tsang, N.-B. Wong, Z. Zhang and S.-T. Lee, *J. Am. Chem. Soc.*, 2007, **129**, 12090–12091.
27 T. Kojima, H. Sugimoto and M. Fujii, *J. Phys. Chem. C*, 2018, **122**, 1874–1880.
28 M. Iqbal, T. K. Purkait, G. G. Goss, J. R. Bolton, M. Gamal El-Din and J. G. Veinot, *ACS Nano*, 2016, **10**, 5405–5412.
29 W. L. Wilson, P. Szajowski and L. Brus, *Science*, 1993, **262**, 1242–1244.
30 T. van Buuren, L. N. Dinh, L. L. Chase, W. J. Siekhaus and L. J. Terminello, *Phys. Rev. Lett.*, 1998, **80**, 3803–3806.
31 J. D. Holmes, K. J. Ziegler, R. C. Doty, L. E. Pell, K. P. Johnston and B. A. Korgel, *J. Am. Chem. Soc.*, 2001, **123**, 3743–3748.
32 D. C. Hannah, J. Yang, P. Podsiadlo, M. K. Y. Chan, A. Demortière, D. J. Gosztola, V. B. Prakapenka, G. C. Schatz, U. Kortshagen and R. D. Schaller, *Nano Lett.*, 2012, **12**, 4200–4205.
33 N. Shirahata, J. Nakamura, J. I. Inoue, B. Ghosh, K. Nemoto, Y. Nemoto, M. Takeguchi, Y. Masuda, M. Tanaka and G. A. Ozin, *Nano Lett.*, 2020, **20**, 1491–1498.
34 D. S. English, L. E. Pell, Z. Yu, P. F. Barbara and B. A. Korgel, *Nano Lett.*, 2002, **2**, 681–685.
35 M. Zacharias, J. Heitmann, R. Scholz, U. Kahler, M. Schmidt and J. Bläsing, *Appl. Phys. Lett.*, 2002, **80**, 661–663.
36 J. G. Veinot, *Chem. Commun.*, 2006, 4160–4168, DOI: **10.1039/b607476f**.
37 S. Godefroo, M. Hayne, M. Jivanescu, A. Stesmans, M. Zacharias, O. I. Lebedev, G. Van Tendeloo and V. V. Moshchalkov, *Nat. Nanotechnol.*, 2008, **3**, 174–178.
38 W. Sun, C. Qian, X. Cui, L. Wang, M. Wei, G. Casillas, A. S. Helmy and G. A. Ozin, *Nanoscale*, 2016, **8**(6), 3678–3684.
39 Y. Yu, G. Fan, A. Fermi, R. Mazzaro, V. Morandi, P. Ceroni, D.-M. Smilgies and B. A. Korgel, *J. Phys. Chem. C*, 2017, **121**, 23240–23248.
40 J. Zhou, J. Huang, H. Chen, A. Samanta, J. Linnros, Z. Yang and I. Sychugov, *J. Phys. Chem. Lett.*, 2021, **12**, 8909–8916.
41 L. Mangolini, E. Thimsen and U. Kortshagen, *Nano Lett.*, 2005, **5**, 655–659.
42 A. Gupta, M. T. Swihart and H. Wiggers, *Adv. Funct. Mater.*, 2009, **19**, 696–703.
43 Z. Li and U. R. Kortshagen, *Chem. Mater.*, 2019, **31**, 8451–8458.
44 Y. Ding, R. Yamada, R. Gresback, S. Zhou, X. Pi and T. Nozaki, *J. Phys. D: Appl. Phys.*, 2014, **47**, 485202.
45 T. A. Pringle, K. I. Hunter, A. Brumberg, K. J. Anderson, J. A. Fagan, S. A. Thomas, R. J. Petersen, M. Sefannaser, Y. Han, S. L. Brown, D. S. Kilin, R. D. Schaller, U. R. Kortshagen, P. R. Boudjouk and E. K. Hobbie, *ACS Nano*, 2020, **14**, 3858–3867.
46 T. Orii, M. Hirasawa and T. Seto, *Appl. Phys. Lett.*, 2003, **83**, 3395–3397.
47 T. Nakamura, Z. Yuan, K. Watanabe and S. Adachi, *Appl. Phys. Lett.*, 2016, **108**, 023105.
48 A. V. Kabashin, A. Singh, M. T. Swihart, I. N. Zavestovskaya and P. N. Prasad, *ACS Nano*, 2019, **13**, 9841–9867.
49 M. Dasog, Z. Yang, S. Regli, T. M. Atkins, A. Faramus, M. P. Singh, E. Muthuswamy, S. M. Kauzlarich, R. D. Tilley and J. G. Veinot, *ACS Nano*, 2013, **7**, 2676–2685.
50 M. Dasog, K. Bader and J. G. C. Veinot, *Chem. Mater.*, 2015, **27**, 1153–1156.
51 R. Sinelnikov, M. Dasog, J. Beamish, A. Meldrum and J. G. C. Veinot, *ACS Photonics*, 2017, **4**, 1920–1929.
52 I. Sychugov, A. Fucikova, F. Pevere, Z. Yang, J. G. C. Veinot and J. Linnros, *ACS Photonics*, 2014, **1**, 998–1005.
53 A. Fucikova, I. Sychugov and J. Linnros, *Faraday Discuss.*, 2020, **222**, 135–148.
54 E. Cartier, J. H. Stathis and D. A. Buchanan, *Appl. Phys. Lett.*, 1993, **63**, 1510–1512.
55 M. Rosso-Vasic, E. Spruijt, B. van Lagen, L. De Cola and H. Zuilhof, *Small*, 2008, **4**, 1835–1841.
56 K. Sato, N. Fukata, K. Hirakuri, M. Murakami, T. Shimizu and Y. Yamauchi, *Chem.– Asian J.*, 2010, **5**, 50–55.
57 J. Yang, R. Liptak, D. Rowe, J. Wu, J. Casey, D. Witker, S. A. Campbell and U. Kortshagen, *Appl. Surf. Sci.*, 2014, **323**, 54–58.
58 J. J. Wu and U. R. Kortshagen, *RSC Adv.*, 2015, **5**, 103822–103828.
59 A. Marinins, R. Zandi Shafagh, W. van der Wijngaart, T. Haraldsson, J. Linnros, J. G. C. Veinot, S. Popov and I. Sychugov, *ACS Appl. Mater. Interfaces*, 2017, **9**, 30267–30272.

60 D. Kajiya and K. I. Saitow, *RSC Adv.*, 2018, **8**, 41299–41307.
61 K. Fujimoto, T. Hayakawa, Y. Xu, N. Jingu and K.-I. Saitow, *ACS Sustainable Chem. Eng.*, 2022, **10**, 14451–14463.
62 K. Q. Loh, H. P. Andaraarachchi, V. E. Ferry and U. R. Kortshagen, *ACS Appl. Nano Mater.*, 2023, **6**, 6444–6453.
63 X. Li, Y. He and M. T. Swihart, *Langmuir*, 2004, **20**, 4720–4727.
64 Z. Yang, C. M. Gonzalez, T. K. Purkait, M. Iqbal, A. Meldrum and J. G. Veinot, *Langmuir*, 2015, **31**, 10540–10548.
65 F. A. Reboredo and G. Galli, *J. Phys. Chem. B*, 2005, **109**, 1072–1078.
66 O. Wolf, M. Dasog, Z. Yang, I. Balberg, J. G. C. Veinot and O. Millo, *Nano Lett.*, 2013, **13**, 2516–2521.
67 D. L. Staebler and C. R. Wronski, *Appl. Phys. Lett.*, 1977, **31**, 292–294.
68 H. Plagwitz, B. Terheiden and R. Brendel, *J. Appl. Phys.*, 2008, **103**, 094506.
69 R. Anthony and U. Kortshagen, *Phys. Rev. B: Condens. Matter Mater. Phys.*, 2009, **80**, 115407.
70 A. N. Thiessen, M. Ha, R. W. Hooper, H. Yu, A. O. Oliynyk, J. G. C. Veinot and V. K. Michaelis, *Chem. Mater.*, 2019, **31**, 678–688.
71 A. N. Thiessen, L. Zhang, A. O. Oliynyk, H. Yu, K. M. O'Connor, A. Meldrum and J. G. C. Veinot, *Chem. Mater.*, 2020, **32**, 6838–6846.
72 R. A. Street, *Adv. Phys.*, 2006, **30**, 593–676.
73 G. D. Cody, T. Tiedje, B. Abeles, B. Brooks and Y. Goldstein, *Phys. Rev. Lett.*, 1981, **47**, 1480–1483.
74 W. Bludau, A. Onton and W. Heinke, *J. Appl. Phys.*, 2003, **45**, 1846–1848.
75 I. T. Cheong, W. Morrish, W. Sheard, H. Yu, B. T. Luppi, L. Milburn, A. Meldrum and J. G. C. Veinot, *ACS Appl. Mater. Interfaces*, 2021, **13**, 27149–27158.
76 C. M. Hessel, E. J. Henderson and J. G. Veinot, *Chem. Mater.*, 2006, **18**, 6139–6146.
77 A. F. van Driel, I. S. Nikolaev, P. Vergeer, P. Lodahl, D. Vanmaekelbergh and W. L. Vos, *Phys. Rev. B: Condens. Matter Mater. Phys.*, 2007, **75**, 035329.
78 J. I. Langford and A. J. C. Wilson, *J. Appl. Crystallogr.*, 1978, **11**, 102–113.
79 P. Yogi, M. Tanwar, S. K. Saxena, S. Mishra, D. K. Pathak, A. Chaudhary, P. R. Sagdeo and R. Kumar, *Anal. Chem.*, 2018, **90**, 8123–8129.
80 B. P. Falcão, J. P. Leitão, M. R. Soares, L. Ricardo, H. Águas, R. Martins and R. N. Pereira, *Phys. Rev. Appl.*, 2019, **11**, 024054.
81 D. A. Kislitsyn, J. M. Mills, S. K. Chiu, B. N. Taber, J. D. Barnes, C. F. Gervasi, A. M. Goforth and G. V. Nazin, *J. Phys. Chem. Lett.*, 2018, **9**, 710–716.
82 L. Canham, *Faraday Discuss.*, 2020, **222**, 10–81.
83 M. L. Mastronardi, F. Maier-Flaig, D. Faulkner, E. J. Henderson, C. Kubel, U. Lemmer and G. A. Ozin, *Nano Lett.*, 2012, **12**, 337–342.
84 M. Nolan, M. Legesse and G. Fagas, *Phys. Chem. Chem. Phys.*, 2012, **14**, 15173–15179.
85 X. D. Pi, L. Mangolini, S. A. Campbell and U. Kortshagen, *Phys. Rev. B: Condens. Matter Mater. Phys.*, 2007, **75**, 085423.
86 X. Liu, Y. Zhang, T. Yu, X. Qiao, R. Gresback, X. Pi and D. Yang, *Part. Part. Syst. Charact.*, 2016, **33**, 44–52.
87 T. L. Cocker, V. Jelic, M. Gupta, S. J. Molesky, J. A. J. Burgess, G. D. L. Reyes, L. V. Titova, Y. Y. Tsui, M. R. Freeman and F. A. Hegmann, *Nat. Photonics*, 2013, **7**, 620–625.
88 T. M. Atkins, A. Thibert, D. S. Larsen, S. Dey, N. D. Browning and S. M. Kauzlarich, *J. Am. Chem. Soc.*, 2011, **133**, 20664–20667.
89 P. Gupta, V. L. Colvin and S. M. George, *Phys. Rev. B: Condens. Matter Mater. Phys.*, 1988, **37**, 8234–8243.
90 P. Martín, J. F. Fernández and C. R. Sánchez, *Phys. Status Solidi A*, 2000, **182**, 255–260.
91 B. N. Jariwala, N. J. Kramer, M. C. Petcu, D. C. Bobela, M. C. M. van de Sanden, P. Stradins, C. V. Ciobanu and S. Agarwal, *J. Phys. Chem. C*, 2011, **115**, 20375–20379.
92 R. Walsh, *Acc. Chem. Res.*, 1981, **14**, 246–252.
93 R. T. Sanderson, *J. Am. Chem. Soc.*, 1983, **105**, 2259–2261.
94 T. M. Hafshejani, J. Wohlgemuth and P. Thissen, *J. Phys. Chem. C*, 2021, **125**, 19811–19820.
95 Y. Shu, U. R. Kortshagen, B. G. Levine and R. J. Anthony, *J. Phys. Chem. C*, 2015, **119**, 26683–26691.
96 Y. Q. Wang, R. Smirani and G. G. Ross, *Nano Lett.*, 2004, **4**, 2041–2045.
97 G. Hadjisavvas, I. N. Remediakis and P. C. Kelires, *Phys. Rev. B: Condens. Matter Mater. Phys.*, 2006, **74**, 165419.
98 H. F. Wilson and A. S. Barnard, *J. Phys. Chem. C*, 2014, **118**, 2580–2586.
99 S. M. Gates, R. R. Kunz and C. M. Greenlief, *Surf. Sci.*, 1989, **207**, 364–384.
100 M. Suemitsu, H. Nakazawa and N. Miyamoto, *Surf. Sci.*, 1996, **357**, 555–559.
101 A. M. Żak, *Nano Lett.*, 2022, **22**, 9219–9226.
102 M. P. Hanrahan, E. L. Fought, T. L. Windus, L. M. Wheeler, N. C. Anderson, N. R. Neale and A. J. Rossini, *Chem. Mater.*, 2017, **29**, 10339–10351.
103 R. N. Pereira, D. J. Rowe, R. J. Anthony and U. Kortshagen, *Phys. Rev. B: Condens. Matter Mater. Phys.*, 2012, **86**, 085449.
104 N. Bushlanova, V. Baturin, S. Lepeshkin and Y. Uspenskii, *Nanoscale*, 2021, **13**, 19181–19189.